Accepted Manuscript

AgP_2/C as an anode for high rate performance lithium-ion batteries

Miao Zhang, Renzong Hu, Jiangwen Liu, Liuzhang Ouyang, Jun liu, Lichun Yang, Fang Fang, Min Zhu

PII: S0925-8388(18)31963-7

DOI: 10.1016/j.jallcom.2018.05.244

Reference: JALCOM 46220

To appear in: *Journal of Alloys and Compounds*

Received Date: 1 March 2018

Revised Date: 3 May 2018

Accepted Date: 21 May 2018

Please cite this article as: M. Zhang, R. Hu, J. Liu, L. Ouyang, Jun liu, L. Yang, F. Fang, M. Zhu, AgP_2/C as an anode for high rate performance lithium-ion batteries, *Journal of Alloys and Compounds* (2018), doi: 10.1016/j.jallcom.2018.05.244.

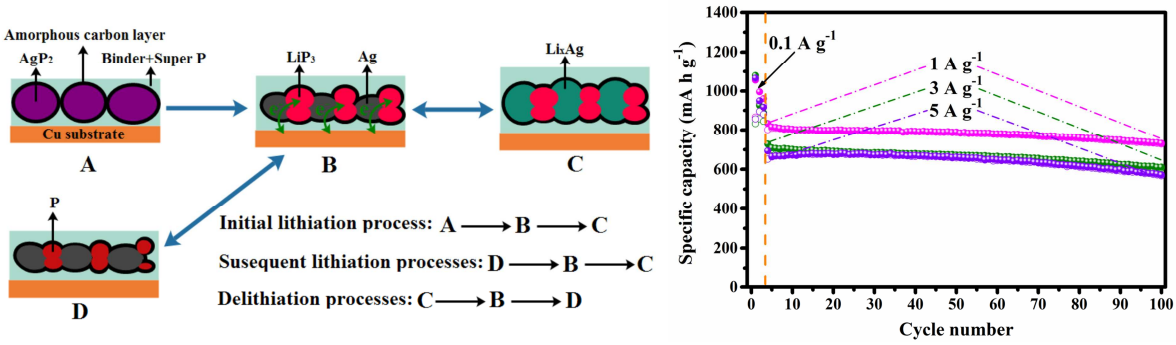

AgP_2/C as an anode for high rate performance lithium-ion batteries

Miao Zhang[a,b], Renzong Hu[a,b], Jiangwen Liu[a,b], Liuzhang Ouyang[a,b]*, Jun liu[a,b], Lichun Yang[a,b],Fang Fang[c,**], Min Zhu[a]

[a] School of Materials Science and Engineering, Guangdong Provincial Key Laboratory of Advanced Energy Storage Materials, South China University ofTechnology, Guangzhou, 510641, PR China

[b] China-Australia Joint Laboratory for Energy & Environmental Materials, Key Laboratory of Fuel Cell Technology of Guangdong Province, Guangzhou,510641, PR China

[c] Department of Materials Science, Fudan University, Shanghai, 200433, PR China

*Corresponding author. E-mail: meouyang@scut.edu.cn (L. Z. Ouyang) & f_fang@fudan.edu.cn

Abstract

Red phosphorus attracts significant interest for lithium-ion batteries due to its high theoretical capacity. Nevertheless, its low electronic conductivity and drastic volume change during cycling limit its further applications. In this study, we fabricate a novel AgP_2/C nanocomposite by facile ball milling. The nanocomposite anode delivers a high reversible capacity of 785mA h g^{-1} at 0.5 A g^{-1} after 100 cycles and an excellent rate capability with a reversible capacity of 605mA h g^{-1} at10 A g^{-1} in half cells. This excellent electrochemical performance is attributed to the uniform dispersion of amorphous carbon and the synergistic effect of intermediate discharge/charge products. In addition, the $LiCoO_2$‖AgP_2/C full cell exhibits a stable capacity with an operation potential of ~2.8 V, indicating the commercial potential of this material in high rate lithium-ion batteries.

Keywords: silver phosphide, anode material, synergistic effect, lithium ion battery

1. Introduction

Commercial lithium-ion batteries (LIBs) are typically composed of lithium metal oxide cathodes and graphite anodes. However, their practical specific energy (~200 Wh kg^{-1}) cannot meet the future demand for high energy storage systems. To significantly improve the specific energy of LIBs, new anode materials with high specific capacities are required.[1-3] Therefore, numerous efforts have been made to explore alternatives to graphite. As one of the possible alternatives, red phosphorus (RP) can react with three Li to form Li_3P and give a high theoretical specific capacity of 2596 mA h g^{-1}. Unfortunately, the low ionic and electronic conductivity within the RP electrode, combined with the drastic volume change (~300%) during lithiation/delithiation processes, results in a low rate capability and poor cycle life.[4-6]

To solve these drawbacks, one effective way is to construct nanostructured P/C nanocomposites with carbon-based materials. The incorporated carbon materials can provide sufficient electrical conductivity and alleviate the volume change during discharge/charge processes, while the constructed nanostructure can shorten Li^+ diffusion paths and reduce stress from the volume change. Until now, two main methods have been employed to construct P/C nanocomposites. One is vaporization-condensation of RP onto various carbon materials and the other is combining RP with carbon into nanocomposites by high energy mechanical milling (HEMM).[7-10] Although these methods can effectively improve the electrochemical performance of RP, the vaporization-condensation process is difficult to control and the electrochemical performance of P/C nanocomposites prepared by HEMM is less than ideal.

On account of this, metal phosphides have drawn considerable attention. This is because the intermediate products of metal elements that are formed *in situ* during the discharge/charge processes can stabilize P and improve the electrical conductivity of the electrode. A number of metal phosphides have been explored, such as FeP,[11] CoP,[12] Ni_2P,[13] MnP[14] and Cu_3P[15]. They react with Li^+ via a conversion reaction, $3yLi^+ + 3ye^{-1} + M_xP_y \longrightarrow yLi_3P + xM$ (M=Fe, Co, Ni or Cu). Since these metals are inactive for Li storage, the theoretical specific capacities of these metal phosphides are relatively low. Therefore, it is of great interest to explore new metal phosphides with reactive metal

components for Li storage. Metallic Ag has the highest electrical conductivity of all the metals and outstanding Li^+ diffusivity, which is beneficial for improving the electrochemical performance of RP.[16] In addition, elemental Ag has a relatively high capacity in a low potential range (0.00–0.25 V).[17]

Herein, we report a metal phosphide AgP_2 anode for LIBs with an impressive theoretical capacity of 1473 mA h g^{-1} while considering a full lithiation of 3 Ag with 10 Li to form $Li_{10}Ag_3$ and P with 3 Li to form Li_3P. It can be obtained by a simple mechanical-chemical reaction of highly conductive Ag and high capacity P. When served as an anode material, it delivers an initial discharge capacity of 1274 mA h g^{-1}, which is higher than the metal phosphides discussed above. By further compositing AgP_2 with carbon black, a new AgP_2/C nanocomposite was obtained. As an electrode material for LIBs, it combines a variety of advantages. First, the *in situ* formed Li_3P serves as a protective matrix to inhibit Ag grain coarsening during cycling. Second, the Ag nanoparticles and amorphous carbon can provide sufficient electrical conductivity and mechanical strength to promote the electrochemical lithiation reaction of P atoms. Third, the nanostructure can reduce the diffusion length of Li^+ and e^-. Thus, the AgP_2/C nanocomposite shows superior electrochemical performance in both half and full cells.

2. Experimental

2.1. Preparation of AgP_2 and AgP_2/C

AgP_2 was synthesized by highenergy shake milling (QM-3C, Nanjing, China) of stoichiometric amounts of Ag (99.9%, 600 mesh, Sinopharm Chemical Reagent Co., Ltd.) and RP (98.5%, Aladdin) powders at 1200 rpm for 3 h under an Ar atmosphere. For comparison, the pure P sample was prepared under the same conditions. The AgP_2/C nanocomposite was synthesized via high energy planetary milling (QM-3SP4, Nanjing, China) of the as-prepared AgP_2 and carbon black (TIMCAL Graphite & Carbon) powders in a mass ratio of 8:2 at 200 rpm for 12 h under an Ar atmosphere. The weight ratio of milling balls to powder was 50:1 for both milling processes.

2.2. Material characterization

XRD patterns of the as-prepared powders were recorded by a PANalytical Empyrean with Cu K_α radiation. Raman spectra were obtained by a HORIBA LabRAM Aramis spectromicroscopy system with a 633 nm wavelength. XPS data were collected with a Thermo Scientific ESCALAB 250 using Al K_α source. SEM and TEM images were observed by Carl Zeiss Supra 40 and JEOL JEM-2100, respectively.

2.3. Electrochemical measurements

The P, AgP_2 and AgP_2/C nanocomposite electrodes were prepared by pasting the slurry containing 70 wt.% of active materials, 15 wt.% of Super P (TIMCAL Graphite & Carbon) and 15 wt.% of carboxymethyl cellulose (CMC, M_w=700000)/styrene butadiene rubber (SBR, BM-451B, Zeon) (1:1 m/m) on copper foil. The load density of the active materials was ~1 mg cm^{-2}. For half cells, the CR2025 coin cells were assembled in an argon-filled glove box with lithium foil as the counter electrode, polyethylene membranes (Teklon@Gold LP) as the separator and a 1 M $LiPF_6$ solution in ethylene carbonate/diethyl carbonate/ethyl methyl carbonate (1:1:1 m/m/m) with 10 wt.% fluoroethylene carbonate as the electrolyte. Galvanostatic charge/discharge experiments were performed at different current rates on a battery testing system (LAND CT2001A). Cyclic voltammetry (CV) over the potential range of 0–2 V at 0.1 mV s^{-1}, and impedance spectra at a 5 mV amplitude signal in a frequency range of 1 MHz to 0.01 Hz, were taken on an electrochemical workstation (Gamry Interface 1000). For the *ex-situ* XRD and TEM analyses, we collected the electrodes by separating the test cells in the argon-filled glove box, washing with DEC several times, and then vacuum dried in the antechamber of the glove box. Full cells were assembled with commercial $LiCoO_2$ electrodes as cathodes and AgP_2/C nanocomposite electrodes as anodes in an argon-filled glove box. The $LiCoO_2$ electrodes consisting of 80:10:10 wt. % of active materials, super P and polyvinylidene fluoride. The CV curves of the full cell were taken between 1.0 and 3.8 V at 0.1 mV s^{-1}. The full cell galvanostatic discharge/charge tests were conducted with a cutoff voltage of 2.0–3.8 V vs Li/Li^+.

3. Results and discussion

The XRD pattern shown in **Fig. 1a** indicates the successful generation of AgP_2 polycrystalline powder after 3 h of high energy shake milling.[18] A weak Ag diffraction peak at 38.2° can be observed in the XRD pattern of AgP_2 powder, this could be due to a small amount of Ag powder adhered to the surface of the ball milling tank, thereby stopping the reaction between Ag and P powders. The consistency between the XRD patterns of AgP_2 and the AgP_2/C nanocomposite indicates no side reactions as a result of high energy planetary milling. The Raman spectrum of the AgP_2/C nanocomposite (insert of **Fig. 1a**) confirms the existence of carbon, with two peaks at ~1350 and ~1590 cm^{-1} belonging to the D (disordered) and G (graphite) bands, respectively.[19] The integral area ratio of the D and G bands is estimated to be 3.29, suggesting the amorphous structure of the carbon in the AgP_2/C nanocomposite. **Fig. 1b** shows the crystal structural model of monoclinic AgP_2. The Ag atoms are in the form of Ag-Ag covalent bonds and are located in the middle of the layers consisting of wrinkled P_{10}^{5-} rings.

Fig. 1c and **d** present the XPS P 2p spectra of AgP_2 and the AgP_2/C nanocomposite. Both of the materials contain two broad peaks located at ~134.3 and ~129.8 eV. The peak located at ~134.3 eV can be attributed to PO_4^{3-} species,[20] resulting from the slight oxidation on the top surface of the powders in air. The peak located at ~129.8 eV can be ideally separated as P $2p_{1/2}$ (~130.5 eV) and $2p_{3/2}$ (~129.5eV). These peaks can be ascribed to AgP_2 due to the binding energy of these peaks being slightly lower than that of elemental phosphorus (P $2p_{1/2}$ ~130.7 eV and $2p_{3/2}$ ~129.8 eV).[21, 22] Upon further analysis, we find that the PO_4^{3-} contribution accounts for 36.5% of the AgP_2 and 82.4% for the AgP_2/C nanocomposite in the surface area, demonstrating a thicker oxidation layer on the surface of the AgP_2/Cnanocomposite.

Furthermore, the microstructure of AgP_2 and the AgP_2/C nanocomposite was investigated by electron microscopy. **Fig. 2a** and **b** show the SEM images of AgP_2 and the AgP_2/C nanocomposite, with untreated commercial Ag and P powders for comparison. The AgP_2 is constituted of dense

particles with sizes from hundreds of nanometers to a few microns. The morphology of the raw materials, including aggregated Ag particles and the bulk size of P particles, disappeared after continuous fracture and welding processes during high energy shake milling.[23] After high energy planetary milling, the AgP_2/C nanocomposite is an aggregation of many sub-micron particles.

Fig. 2c and **d** exhibit the HRTEM images of AgP_2 and the AgP_2/C nanocomposite. Both images reveal the clear lattice fringes corresponding to the $(\bar{1}12)$ and $(\bar{1}13)$ planes of AgP_2. Compared with AgP_2, the AgP_2/C nanocomposite has a much smaller crystalline grain size and more amorphous interfacial regions. Further observations reveal that the AgP_2 particles are surrounded by amorphous carbon in the AgP_2/C nanocomposite. In addition, consistent with the XRD results, both samples show clear polycrystalline rings corresponding to the $(\bar{1}12)$, $(\bar{1}13)$ and (300)/ (202) planes of AgP_2 in selected area electron diffraction (SAED) patterns. Elemental mapping under scanning transmission electron microscopy (STEM), as shown in **Fig. 2e-h**, displays the homogeneous distribution of Ag, P and C in the sample, indicating the uniform coating of the carbon layer.

Fig. 3a shows the initial discharge/charge curves of P, AgP_2 and the AgP_2/C nanocomposite at a current density of 0.1 A g^{-1}. It can be seen that the P electrode shows the highest discharge capacity of 2535 mA h g^{-1}, but with a poor Coulombic efficiency of 4.18%. In comparison, the initial discharge capacity of the AgP_2 electrode is decreased to 1274 mA h g^{-1}, although a higher initial Coulombic efficiency of 72.6% is achieved. The significantly improved initial Coulombic efficiency may be attributed to the enhancement of electrical conductivity of the AgP_2 electrode. Compare to the AgP_2 electrode, due to the existence of amorphous carbon in the AgP_2/C nanocomposite, the initial discharge capacity of the AgP_2/C nanocomposite electrode is decreased ~200 mA h g^{-1}, but with a relative higher initial Coulombic efficiency of 78.3% achieved. The increased Coulombic efficiency of the AgP_2/C nanocomposite electrode can be attributed to the amorphous carbon network, which not only improves the conductivity of the electrode but also reduces the direct conduct between AgP_2 particles and the electrolyte.

The electrochemistry impedance spectra measurements were performed after the first cycle at 2 V to compare the conductivity of the three electrodes. As presented in **Fig. 3b**, the semicircle in the medium-to-low frequency region corresponds to charge-transfer resistance (Rct) and the inclined line in the low-frequency region can be attributed to Li^+ diffusion in the electrode.[24] The value of the Rct was obtained by fitting the EIS using an equivalent circuit. It has been found that the Rct values of the P, AgP_2 and AgP_2/C nanocomposite electrodes are 245.8, 61.7 and 35.7 Ω, respectively, indicating the highest e^- transfer rate in the AgP_2/C nanocomposite electrode.

Fig. 3c compares the cycling performance of the AgP_2 and AgP_2/C nanocomposite electrodes. The capacity of the AgP_2 electrode decreased to 541 mA h g^{-1} after 100 cycles. In contrast, in the AgP_2/C nanocomposite electrode, the uniform carbon layer not only enhances the electrical conductivity of the electrode, but also alleviates the volume change of active materials during cycling. Furthermore, the small particle size after planetary milling can alleviate the absolute volume change and reduce the Li^+ diffusion length, this results in a relatively higher capacity of 785 mA h g^{-1} for the AgP_2/C nanocomposite after 100 cycles.

In addition, the AgP_2/C nanocomposite electrode also presents excellent rate capability. As shown in **Fig. 3d**, the reversible capacities are 843,745, 677, 651, 620 and 605 mAh g^{-1} at 0.1, 1, 3, 5, 8 and 10 A g^{-1}, respectively. When the current density returns to 0.1 A g^{-1}, a reversible capacity of 777 mAh g^{-1} can be recovered, indicating the good reversibility of the AgP_2/C nanocomposite. **Fig. 3e** indicates that the AgP_2/C nanocomposite has higher superior rate capability than other reported metal phosphides.[13, 25-32] Furthermore, the AgP_2/C nanocomposite electrode exhibits good cycling performance even at high current densities. As presented in **Fig. 3f**, all electrodes were tested at 0.1 A g^{-1} for the initial three cycles and then different current densities for the following cycles. When cycling at a current density of 1 A g^{-1}, the AgP_2/C nanocomposite slowly decreases from 834 to 731 mA h g^{-1}. Further increases the current density to 3 A g^{-1}, although it shows relacively lower reversible capacities, a good capacity retention still can be achieved, for it just decline ~100 mAh/g during 97 cycles and obtain a discharge capacity of 611 mA h g^{-1} at the end of 100 cycles. While at a current density of 5 A g^{-1}, it shows the lowest reversibe capacities, however, the discharge capacity can still

remain as high as 572 mA h g^{-1} after 100 cycles with 82.5% retention of the initial discharge capacity at 5 A g^{-1} (693 mA h g^{-1}), indicating high rate capabiity for the AgP_2/C nanocomposite electrode.

In order to gain more information regarding the electrochemical reaction processes of the AgP_2/C nanocomposite, we performed CV, *ex-situ* XRD, *ex-situ* HRTEM and SAED analyses on the discharge/charge electrode. As shown in **Fig. 4a**, during the initial cathodic scan, the broad peak from 0.4 to 0.8 V can be ascribed to the conversion reaction between Li and AgP_2 to form Ag and LiP_3. Then, the potential below 0.2 V is believed to be the alloy reaction between Li and elemental Ag.[16] After first cycle, three peaks located from 0.4 to 1.2 V are consistent with the cathodic peaks of elemental P.[4, 5] In the reverse sweeps, two small oxidation peaks located at 0.1 and 0.3 V can be ascribed to the dealloying reaction of Ag with Li,[33] while the anodic peaks from 1.0 to 1.5 V correspond to stepwise Li extraction from Li_3P.[8] In addition, no obvious shifts are observed from the second cycle, indicating the good cycling stability of the AgP_2/C nanocomposite.

To confirm this mechanism, we performed *ex-situ* XRD measurements of the AgP_2/C nanocomposite electrodes at seven different discharge/charge states during the first cycle. As shown in **Fig. 4b** and **c**, the characteristic peaks of the AgP_2 phase disappeared after discharge to 0.3 V, while the Ag signals increased their intensities and the XRD peaks of Li_3P are observed. As the potential lowered further to 0.1 V, the metallic Ag alloyed with Li to form LiAg (cubic), LiAg (tetragonal) and Li_9Ag_4 phases. When the electrode fully discharged to a terminate voltage of 0.01 V, the XRD pattern shows the presence of Li_3P and $Li_{10}Ag_3$. Upon reversed charging to 0.8 V, the Li-Ag alloy phases completely convert to elemental Ag. After further charging to 1.2 V, the Li_3P phase is partially delithiated to form a new LiP_7 phase. When the electrode is fully charged, only the Ag phase peaks are detected, this result illustrates that AgP_2 cannot be regenerated after initial discharge/charge processes. According to the above analysis, the reaction mechanism of AgP_2 can be described as follows:

During the initial lithiation process:

$$AgP_2 \longrightarrow Ag + Li_3P \longrightarrow Li_{10}Ag_3 + Li_3P$$

During subsequent delithiation and lithiation processes:

$Li_{10}Ag_3 \longleftrightarrow Ag$

$Li_3P \longleftrightarrow P$

To gain more information into the phasecomposition and distribution of the AgP_2/C nanocomposite during cycling, the reaction products of fully lithiated AgP_2/C to 0.01 V and fully delithiated AgP_2/C at 2 V were investigated by HRTEM and SEAD. **Fig. 4d** shows the *ex-situ* HRTEM and SAED images of the lithiated (discharged) AgP_2/C nanocomposite. The HRTEM image clearly shows the coexistence of the (411) plane of Li_3Ag_{10} and the (011) plane of Li_3P with the lattice fringes of ~0.235 and ~0.333 nm, respectively. The two phases are uniformly distributed in the amorphous carbon matrix. The corresponding SAED pattern further confirms the existence of Li_3Ag_{10} and Li_3P nanocrystals. After charging to 2 V, the HRTEM image (**Fig. 4e)** exhibits ultrafine Ag nanoparticles that are highly dispersed in the amorphous P/C host matrix. Furthermore, in agreement with the *ex-situ* XRD results, the SAED pattern only shows the multiple rings of the Ag phase. In the following 10^{th}, 30^{th}, 50^{th} and 100^{th} cycles, the Ag phasesdo not tend to coarsen to form large grains, which is reflected by their lack of significantly changed diffraction peaks in **Fig. 4f**.

On basis of the above analysis, a schematic illustration is given to summarize the electrochemical reaction processes. As illustrated in **Fig. 4g**, the intermediate discharge/charge products of the AgP_2/C nanocompositeare combined to give a synergistic effect during cycling. The *in-situ* formed Li_3P phase serves as a shielding matrix to prevent the Ag grains coarsening during cycling, while the highly dispersed Ag nanoparticles and amorphous carbon network act as electronic pathways and buffer the matrix to promote reversible Li storage reaction of the P component.

As a result of its good electrochemical performance in half cells, the AgP_2/C nanocomposite was further tested in full cells with $LiCoO_2$ as the cathode. **Fig. 5a** shows that the pouch-type $LiCoO_2$‖AgP_2/C full cell is able to drive a SCUT icon fan.We then conducted CV and galvanostatic discharge/charge measurements with coin-type cells. **Fig. 5b** shows the CV curves of the $LiCoO_2$‖AgP_2/C full cell at a scanning rate of 0.1 mV s^{-1} between 1.0 and 3.8V. During the initial charging process, the main peaks from 2.8 to 3.5 V can be attributed to the Li^+ extraction of $LiCoO_2$

and reaction with AgP_2. In subsequent cycles, these peaks are shifted to a lower potential due to the reduced electrode polarization after initial activation of theAgP_2/C electrode. In the reverse scan, the dominant peaks between 2.3 and 3.0 V can be ascribed to the delithiation ofLi_3P and lithiation of $Li_{1-x}CoO_2$.

According to the CV results, we chose 2.0–3.8 V as the cutoff voltage to conduct galvanostatic discharge/charge tests. **Fig.5c** and **d** show the voltage profiles and cycling performance of the $LiCoO_2$‖AgP_2/C full cells at a current density of 0.1 A g^{-1} for the initial three cycles and 0.5 A/g for the subsequent cycles. The operation potential of this cell is ~2.8 V, which is higher than $LiTi_5O_{12}$/$LiFePO_4$ (2.0 V). However, the initial charge capacity (723 mA h g^{-1} vs. anode) and Coulombic efficiency (64% vs. anode) in the full cells are much less than in the half cells. Despite all this, the anode electrode still shows high capacity (431 mA h g^{-1}) after 100 cycles. The lower initial Coulombic efficiency and capacities may be caused by many factors, such as the limited cut-off voltages of the cell and unmatched capacity ratio of the two electrodes. We will do in-depth research into these points and give results in future work.

4. Conclusions

In summary, we have successfully synthesized a new AgP_2/C nanocomposite anode via a simple mechanochemical reaction of metallic Ag, elemental P and carbon black. The as-prepared AgP_2/C nanocomposite anode exhibits high reversible capacities, excellent rate capability and superior cycling stability in half cells. These excellent electrochemical performances are attributed to the uniformly distributed carbon matrix and synergistic Li-storage reactions of Ag and P components, where the *in-situ* formed Li_3P phase serve as a shielding matrix to prevent the aggregation and alleviate the volume change of Ag nanoparticles during cycling, while the highly dispersed Ag nanoparticles act as electronic pathways and buffer matrix to promote the reversible Li storage reaction of P component. In addition, the anode electrode shows higher capacity than graphite in a $LiCoO_2$‖AgP_2/C full cell, indicating the commercial potential of this material.

Acknowledgements

This work was supported by the International Science & TechnologyCooperation Program of China (2015DFA51750) andFoundation for Innovative Research Groups of the National Natural Science Foundation of China (No. NSFC51621001), the National Natural Science Foundation of China Projects (No. 51431001and 51771075) and by the Natural Science Foundation of Guangdong Province of China (Nos. 2016A030312011). We also acknowledge the support of the Guangdong Province Universities and Colleges Pearl River Scholar Funded Scheme (2014).

References

[1] J.B. Goodenough, K.S. Park, The Li-Ion Rechargeable Battery: A Perspective, J. Am. Chem. Soc. 135 (2013) 1167-1176.

[2] J. Sun, G. Zheng, H.W. Lee, N. Liu, H. Wang, H. Yao, W. Yang, Y. Cui, Formation of Stable Phosphorus−Carbon Bond for Enhanced Performance in Black Phosphorus Nanoparticle-Graphite Composite Battery Anodes, Nano Lett. 14 (2014) 4573-4580.

[3] R. Hu, Y. Ouyang, T. Liang, H. Wang, J. Liu, J. Chen, C. Yang, L. Yang, M. Zhu, Stabilizing the Nanostructure of SnO_2 Anodes by Transition Metals: A Route to Achieve High Initial Coulombic Efficiency and Stable Capacities for Lithium Storage, Adv. Mater. 29 (2017) 1605006.

[4] W. Li, Z. Yang, M. Li, Y. Jiang, X. Wei, X. Zhong, L. Gu, Y. Yu, Amorphous Red Phosphorus Embedded in Highly Ordered Mesoporous Carbon with Superior Lithium and Sodium Storage Capacity, Nano lett. 16 (2016) 1546-1553.

[5] D. Yuan, J. Cheng, G. Qu, X. Li, W. Ni, B. Wang, H. Liu, Amorphous red phosphorous embedded in carbon nanotubes scaffold as promising anode materials for lithium-ion batteries, J. Power Sources 301 (2016) 131-137.

[6] M. Zhang, R. Hu, J. Liu, L. Ouyang, J. Liu, L. Yang, M. Zhu, A $ZnGeP_2$/C anode for lithium-ion and sodium-ion batteries, Electrochem. Commun. 77 (2017) 85-88.

[7] L. Wang, X. He, J. Li, W. Sun, J. Gao, J. Guo, C. Jiang, Nano-Structured Phosphorus Composite as High-Capacity Anode Materials for Lithium Batteries, Angew. Chem. Int. Ed. 51 (2012) 9034-9037.

[8] W. Li, Z. Yang, Y. Jiang, Z. Yu, L. Gu, Y. Yu, Crystalline red phosphorus incorporated with porous carbon nanofibers as flexible electrode for high performance lithium-ion batteries, Carbon 78 (2014) 455-462.

[9] C. Marino, L. Boulet, P. Gaveau, B. Fraisse, L. Monconduit, Nanoconfined phosphorus in mesoporous carbon as an electrode for Li-ion batteries: performance and mechanism, J. Mater. Chem. 22 (2012) 22713-22720.

[10] C.M. Park, H.J. Sohn, Black Phosphorus and its Composite for Lithium Rechargeable Batteries, Adv. Mater. 19 (2007) 2465-2468.

[11] M. Pramanik, Y. Tsujimoto, V. Malgras, S.X. Dou, J.H. Kim, Y. Yamauchi, Mesoporous Iron Phosphonate Electrodes with Crystalline Frameworks for Lithium-Ion Batteries, Chem. Mater. 27 (2015) 1082-1089.

[12] X. Xu, J. Liu, R. Hu, J. Liu, L. Ouyang, M. Zhu, Self-Supported CoP Nanorod Arrays Grafted on Stainless Steel as an Advanced Integrated Anode for Stable and Long-Life Lithium-Ion Batteries, Chem. Eur. J. 23 (2017) 5198-5204.

[13] C. Wu, P. Kopold, P.A. van Aken, J. Maier, Y. Yu, High Performance Graphene/Ni_2P Hybrid Anodes for Lithium and Sodium Storage through 3D Yolk-Shell-Like Nanostructural Design, Adv. Mater. 29 (2017) 1604015.

[14] L. Li, Y. Peng, H. Yang, Phase structure changes of MnP anode material during electrochemical lithiation and delithiation process, Electrochim. Acta 95 (2013) 230-236.

[15] M.C. Stan, R. Klöpsch, A. Bhaskar, J. Li, S. Passerini, M. Winter, Cu_3P Binary Phosphide: Synthesis via a Wet Mechanochemical Method and Electrochemical Behavior as Negative Electrode Material for Lithium-Ion Batteries, Adv. Energy Mater. 3 (2013) 231-238.

[16] C.-M. Park, H. Jung, H.-J. Sohn, Electrochemical Behaviors and Reaction Mechanism of Nanosilver with Lithium, Electrochem. Solid St. 12 (2009) A171-A175.

[17] G. Taillades, J. Sarradin, Silver: high performance anode for thin film lithium ion batteries, J.Power Sources 125 (2004) 199-205.

[18] Von M.H. Möuller, W. Jeitschko, Darstellung, Eigenschaften und Kristallstruktur von Cu_2P_7 und Strukturverfeinerungen von CuP_2 und AgP_2, Z. anorg. allg. Chem. 491 (1982) 225-236.

[19] H. Kim, B. Han, J. Choo, J. Cho, Three-Dimensional Porous Silicon Particles for Use in High-Performance Lithium Secondary Batteries, Angew. Chem. 47 (2008) 10151-10154.

[20] P. Perez-Romo, C. Potvin, J.M. Manoli, M.M. Chehimi, G. Djéga-Mariadassou, Phosphorus-Doped Molybdenum Oxynitrides and Oxygen-Modified Molybdenum Carbides: Synthesis, Characterization, and Determination of Turnover Rates for Propene Hydrogenation, J. Catal. 208 (2002) 187-196.

[21] J. Song, Z. Yu, M.L. Gordin, S. Hu, R. Yi, D. Tang, T. Walter, M. Regula, D. Choi, X. Li, A. Manivannan, D. Wang, Chemically Bonded Phosphorus/Graphene Hybrid as a High Performance Anode for Sodium-Ion Batteries, Nano lett. 14 (2014) 6329-6335.

[22] S.O. Kim, A. Manthiram, The facile synthesis and enhanced sodium-storage performance of a chemically bonded CuP2/C hybrid anode, Chem. Commun. 52 (2016) 4337-4340.

[23] C. Suryanarayana, N. Al-Aqeeli, Mechanically alloyed nanocomposites, Prog. Mater. Sci. 58 (2013) 383-502.

[24] W. Sun, R. Hu, H. Liu, H. Zhang, J. Liu, L. Yang, H. Wang, M. Zhu, Silicon/Wolfram Carbide@Graphene composite: enhancing conductivity and structure stability in amorphous-silicon for high lithium storage performance, Electrochim. Acta 191 (2016) 462-472.

[25] J. Yang, Y. Zhang, C. Sun, H. Liu, L. Li, W. Si, W. Huang, Q. Yan, X. Dong, Graphene and cobalt phosphide nanowire composite as an anode material for high performance lithium-ion batteries, Nano Res. 9 (2016) 612-621.

[26] X. Wang, K. Chen, G. Wang, X. Liu, H. Wang, Rational Design of Three-Dimensional Graphene Encapsulated with Hollow FeP@Carbon Nanocomposite as Outstanding Anode Material for Lithium Ion and Sodium Ion Batteries, ACS Nano 11 (2017) 11602-11616.

[27] S. Liu, X. He, J. Zhu, L. Xu, J. Tong, Cu_3P/RGO Nanocomposite as a New Anode for Lithium-Ion Batteries, Sci. Rep. 6 (2016) 35189.

[28] J. Yang, Y. Ouyang, H. Zhang, H. Xu, Y. Zhang, Y. Wang, Novel Fe_2P/graphitized carbon yolk/shell octahedra for high-efficiency hydrogen production and lithium storage, J. Mater. Chem. A 4 (2016) 9923-9930.

[29] X. Wang, P. Sun, J. Qin, J. Wang, Y. Xiao, M. Cao, A three-dimensional porous MoP@C hybrid as a high-capacity, long-cycle life anode material for lithium-ion batteriesl, Nanoscale 8 (2016) 10330-10338.

[30] J. Jiang, C. Wang, W. Li, Q. Yang, One-pot synthesis of carbon-coated Ni5P4 nanoparticles and CoP nanorods for high-rate and high-stability lithium-ion batteries J. Mater. Chem. A 3 (2015) 23345-23351.

[31] A. Lu, X. Zhang, Y. Chen, Q. Xie, Q. Qi, Y. Ma, D.-L. Peng, Synthesis of Co_2P/graphene nanocomposites and their enhanced properties as anode materials for lithium ion batteries, J. Power Sources 295 (2015) 329-335.

[32] S. Liu, H. Zhang, L. Xu, L. Ma, X. Chen, Solvothermal preparation of tin phosphide as a long-life anode for advanced lithium and sodium ion batteries, J. Power Sources 304 (2016) 346-353.

[33] P. Li, H. Lan, L. Yan, S. Qian, H. Yu, X. Cheng, N. Long, M. Shui, J. Shu, Lithiation/Delithiation Behavior of Silver Nitrate as Lithium Storage Material for Lithium Ion Batteries, ACS Sustainable Chem. Eng. 5 (2017) 5686-5693.

Figure caption

Fig. 1 (a) XRD patterns of the AgP_2 and AgP_2/C nanocomposite (insert shows Raman spectrum of the AgP_2/C nanocomposite), (b) structural demonstration of the monoclinic AgP_2, (c) XPS P 2p spectrum of the AgP_2 and (d) XPS P 2p spectrum of the AgP_2/C nanocomposite.

Fig. 2 SEM images of (a) the AgP_2 and (b) AgP_2/C nanocomposite (the insets of Fig. 2a are SEM images of Ag and P powers), TEM images of (c) the AgP_2 and (d) AgP_2/C nanocomposite (the insets are corresponding SEAD patterns), (e) STEM image and (f-h) element mapping images of the AgP_2/C nanocomposite.

Fig. 3 Galvanostalic discharge/charge profiles of (a) the AgP_2 and AgP_2/C nanocomposite at a current density of 0.1 A/g, (b) Nyquist plots of the AgP_2 and AgP_2/C nanocomposite at fully charged state after the first cycle (the inset is corresponding to equivalent circuit), (c) cycling performance of the AgP_2 and AgP_2/C nanocomposite electrodes, all electrodes were tested at a current density of 0.1 A g^{-1} for the initial three cycles and then 0.5 A/g for the following cycles, (d) rate capability of the AgP_2/C nanocomposite, (e) comparison of rate capability of AgP2/C composites with other reported metal phosphides and (f) capacity vs. cycle number of the AgP_2/C nanocomposite at different current rates (0.1 A g^{-1} for the initial three cycles).

Fig. 4 (a) CV curves of the AgP_2/C nanocomposite electrode at a scanning rate of 0.1 mV s^{-1}, (b) initial potential *vs.* capacity curve of the AgP_2/C nanocompositewith seven electrochemical reaction states for *ex-situ* XRD measurements, namely open cell potential (OCP), discharge to 0.3, 0.1 and 0.01 V, recharged to 0.8, 1.2 and 2.0 V, (c) *ex-situ* XRD patterns of the AgP_2/C nanocompositeelectrodeat seven different states for the first cycle, *ex-situ* HRTEM and SEAD images of the AgP_2/C nanocomposite electrodes after (d) discharge to 0.01 V and (e) charge to 2 V, (f) comparison *ex-situ* XRD patterns of the AgP_2/C nanocomposite electrodes at fully charged state for different cycles (1^{st},

10^{th}, 30^{th}, 50^{th} and 100^{th}) and (g) a schematic illustrationof the electrochemical reaction processes of the AgP_2/C nanocomposite electrode.

Fig. 5 (a) Optical imagesof a SCUT icon fan driven by the pouch-type $LiCoO_2$‖AgP_2/C full cell, (b) CV curves of the $LiCoO_2$‖AgP_2/C full cell and $LiCoO_2$ electrode with a scanning rate of 0.1 mV s^{-1}, (c) galvanostatic discharge/charge profiles and (d) cycling performance of the $LiCoO_2$‖AgP_2/C full cells in the voltage window of 2.0-3.8 V. The above cells were tested at a current density of 0.1 A g^{-1} for the first three cycles and 0.5 A/g for the subsequent cycles.

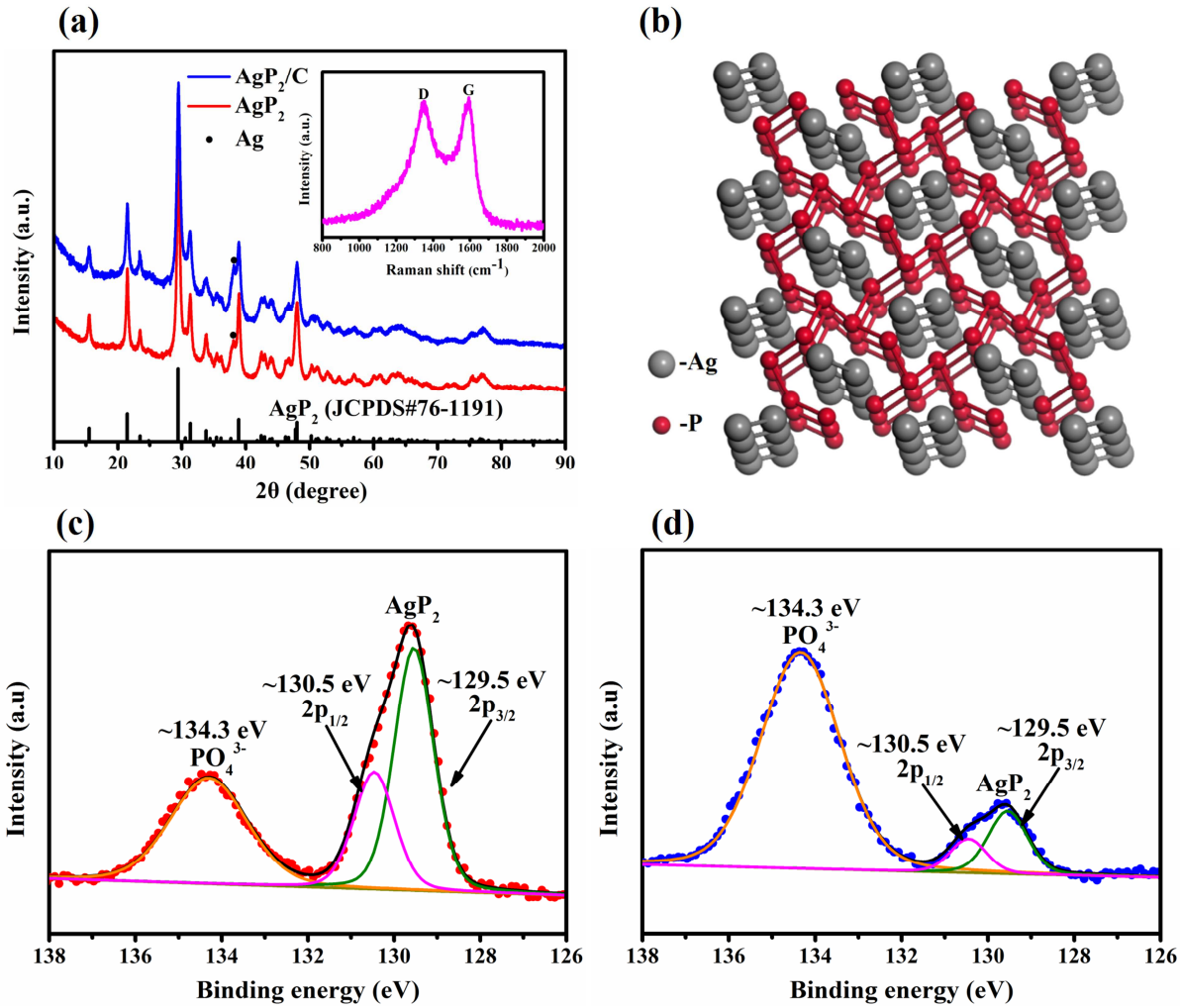
(a)
AgP2/C
AgP2
Ag
Intensity (a.u.)
D
G
Raman shift (cm-1)
AgP2 (JCPDS#76-1191)
2θ (degree)
(b)
-Ag
-P
(c)
AgP2
~134.3 eV
PO4 3-
~130.5 eV
2p1/2
~129.5 eV
2p3/2
Intensity (a.u)
Binding energy (eV)
(d)
~134.3 eV
PO4 3-
~130.5 eV
2p1/2
AgP2
~129.5 eV
2p3/2
Intensity (a.u)
Binding energy (eV)

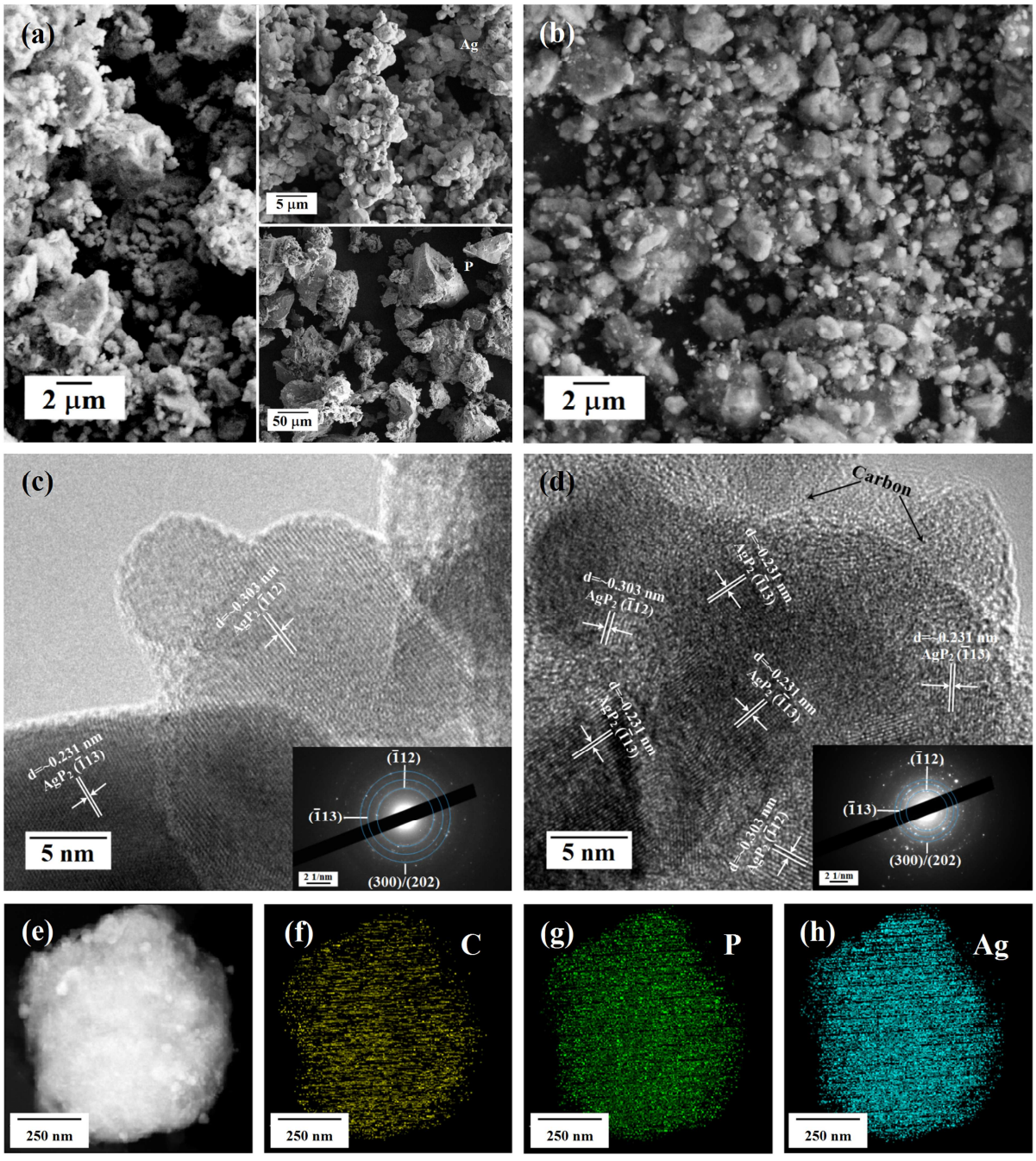
(a)
Ag
5 μm
P
50 μm
2 μm
(b)
2 μm
(c)
d=0.302 nm
AgP2 (1̄12)
d=0.231 nm
AgP2 (1̄13)
5 nm
(1̄12)
(1̄13)
(300)/(202)
2 1/nm
(d)
Carbon
d=0.303 nm
AgP2 (1̄12)
d=0.231 nm
AgP2 (1̄13)
d=0.231 nm
AgP2 (1̄13)
d=0.231 nm
AgP2 (1̄13)
d=0.231 nm
AgP2 (1̄13)
d=0.303 nm
AgP2 (1̄12)
5 nm
(1̄12)
(1̄13)
(300)/(202)
2 1/nm
(e)
250 nm
(f)
C
250 nm
(g)
P
250 nm
(h)
Ag
250 nm

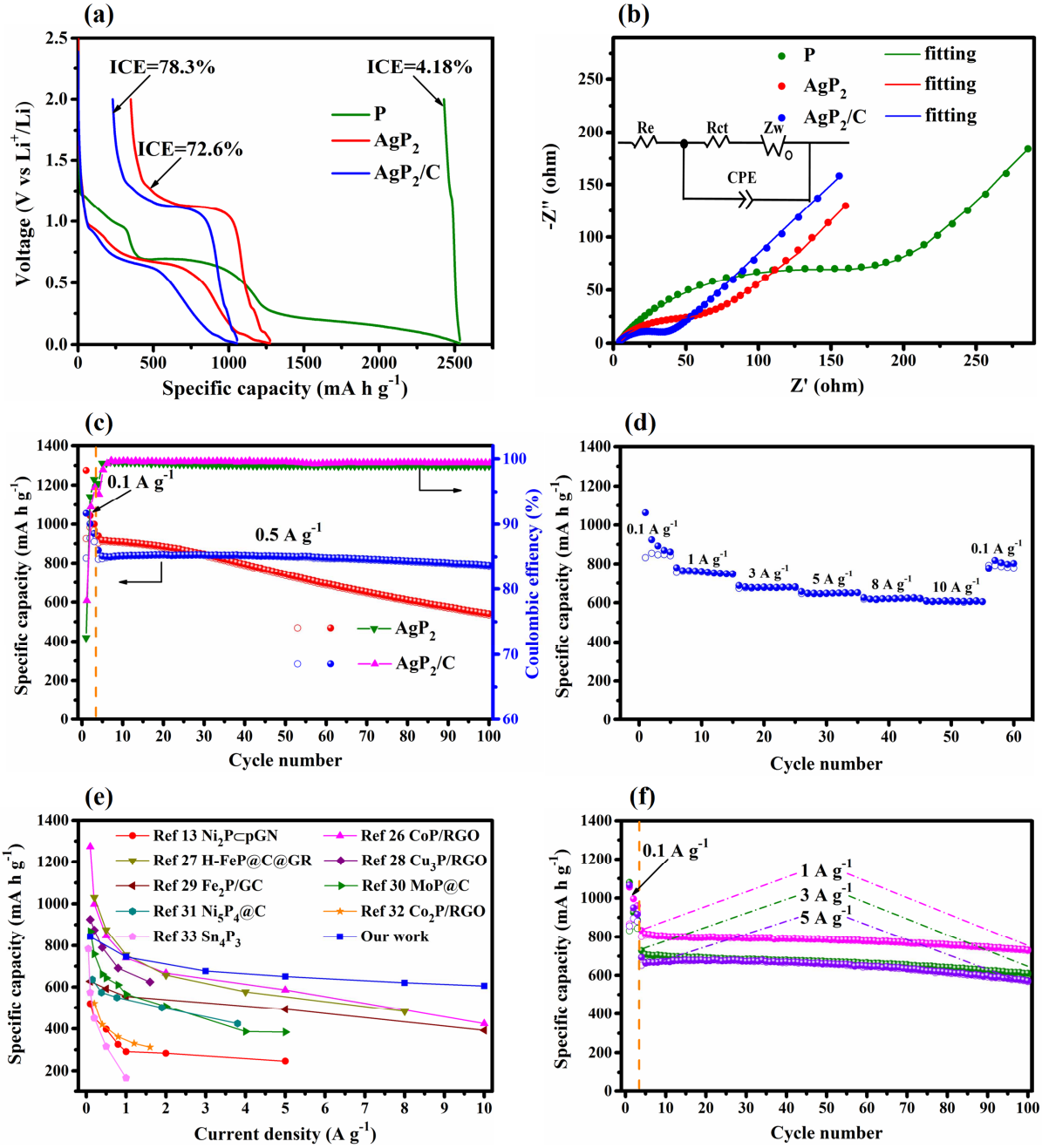
(a)
ICE=78.3%
ICE=72.6%
ICE=4.18%
P
AgP2
AgP2/C
Voltage (V vs Li+/Li)
Specific capacity (mA h g-1)
(b)
P
AgP2
AgP2/C
fitting
fitting
fitting
Re
Rct
Zw
CPE
-Z'' (ohm)
Z' (ohm)
(c)
0.1 A g-1
0.5 A g-1
AgP2
AgP2/C
Specific capacity (mA h g-1)
Coulombic effiency (%)
Cycle number
(d)
0.1 A g-1
1 A g-1
3 A g-1
5 A g-1
8 A g-1
10 A g-1
0.1 A g-1
Specific capacity (mA h g-1)
Cycle number
(e)
Ref 13 Ni2P⊂pGN
Ref 26 CoP/RGO
Ref 27 H-FeP@C@GR
Ref 28 Cu3P/RGO
Ref 29 Fe2P/GC
Ref 30 MoP@C
Ref 31 Ni5P4@C
Ref 32 Co2P/RGO
Ref 33 Sn4P3
Our work
Specific capacity (mA h g-1)
Current density (A g-1)
(f)
0.1 A g-1
1 A g-1
3 A g-1
5 A g-1
Specific capacity (mA h g-1)
Cycle number

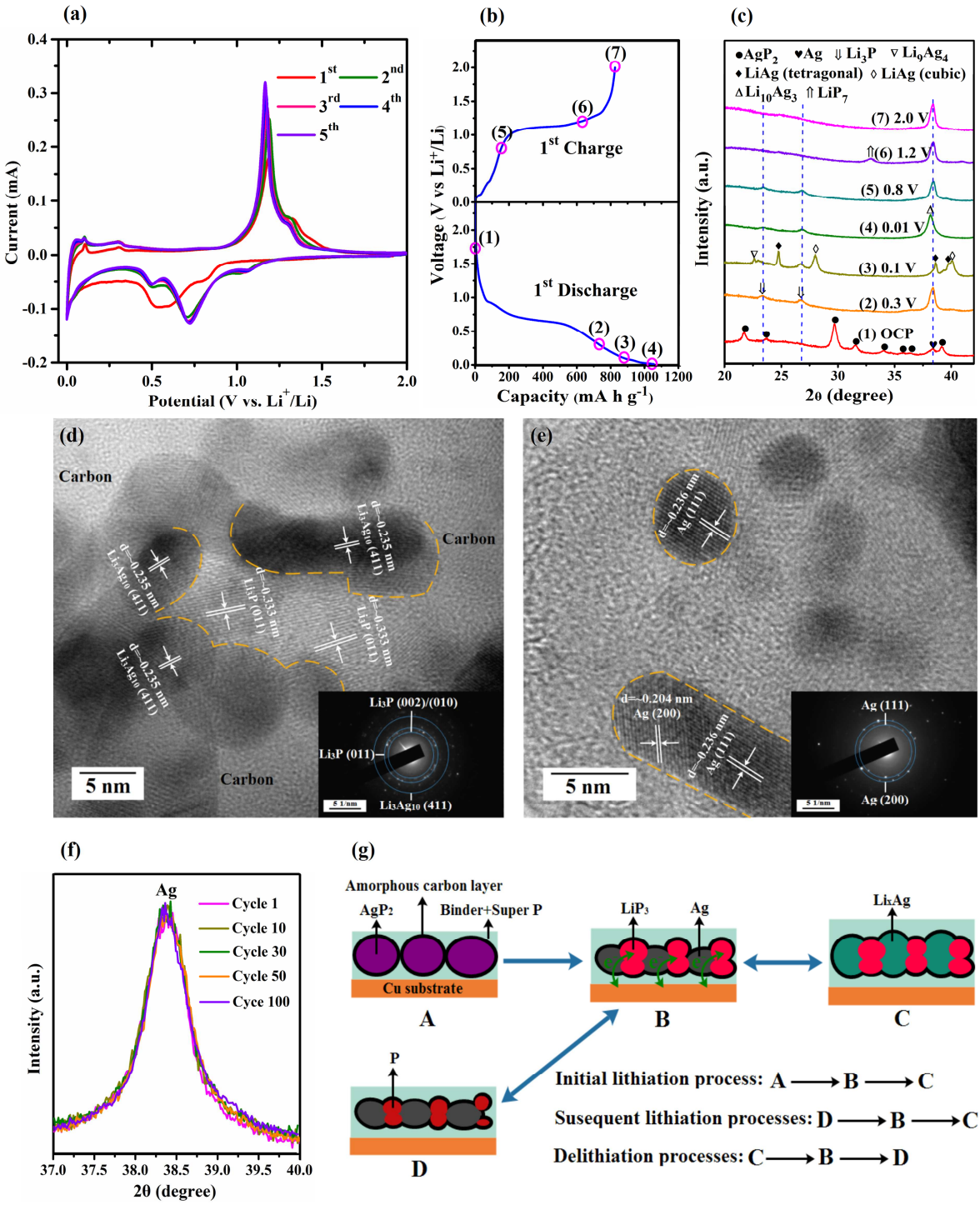
(a)
Current (mA)
Potential (V vs. Li+/Li)
1st
2nd
3rd
4th
5th
(b)
Voltage (V vs Li+/Li)
Capacity (mA h g-1)
1st Charge
1st Discharge
(1)
(2)
(3)
(4)
(5)
(6)
(7)
(c)
●AgP2 ♥Ag ⇓Li3P ▽Li9Ag4
♦LiAg (tetragonal) ◊LiAg (cubic)
▵Li10Ag3 ⇑LiP7
(7) 2.0 V
⇑(6) 1.2 V
(5) 0.8 V
(4) 0.01 V
(3) 0.1 V
(2) 0.3 V
(1) OCP
Intensity (a.u.)
2θ (degree)
(d)
Carbon
Carbon
Carbon
d=~0.235 nm Li3Ag10 (411)
d=~0.333 nm Li3P (011)
Li3P (002)/(010)
Li3P (011)
Li3Ag10 (411)
5 nm
(e)
d=~0.236 nm Ag (111)
d=~0.204 nm Ag (200)
Ag (111)
Ag (200)
5 nm
(f)
Ag
Cycle 1
Cycle 10
Cycle 30
Cycle 50
Cyce 100
Intensity (a.u.)
2θ (degree)
(g)
Amorphous carbon layer
AgP2
Binder+Super P
Cu substrate
LiP3
Ag
LixAg
A
B
C
P
D
Initial lithiation process: A → B → C
Susequent lithiation processes: D → B → C
Delithiation processes: C → B → D

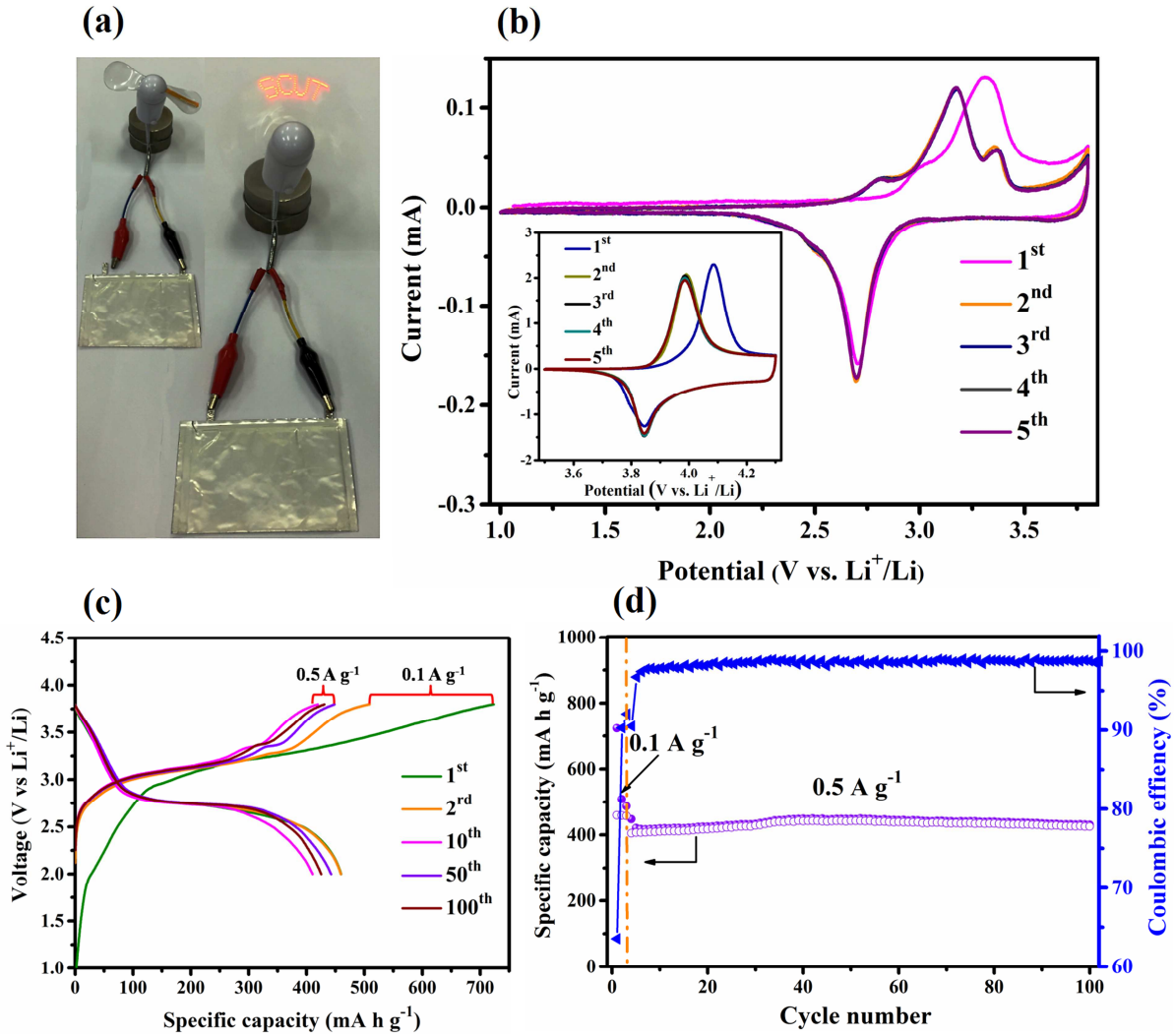
(a)
(b)
Current (mA)
Potential (V vs. Li+/Li)
1st
2nd
3rd
4th
5th
(c)
Voltage (V vs Li+/Li)
Specific capacity (mA h g-1)
0.5 A g-1
0.1 A g-1
1st
2nd
10th
50th
100th
(d)
Specific capacity (mA h g-1)
Coulombic effiency (%)
Cycle number
0.1 A g-1
0.5 A g-1

Highlights

• We have successfully synthesized AgP_2 and AgP_2/C composite powders for lithium ion batteries.

• The AgP_2/C composite has not been reported in use of lithium-ion batteries.

• The AgP_2/C composite demonstrates excellent electrochemical performance for both half and full cells.

• The method is high yield, low-cost and environmentally friendly.